



HAL
open science

Intrinsic and Atmospherically Forced Variability of the AMOC: Insights from a Large-Ensemble Ocean Hindcast

Stephanie Leroux, Thierry Penduff, Laurent Bessières, Jean-Marc Molines, Jean-Michel Brankart, Guillaume Sérazin, Bernard Barnier, Laurent Terray

► To cite this version:

Stephanie Leroux, Thierry Penduff, Laurent Bessières, Jean-Marc Molines, Jean-Michel Brankart, et al.. Intrinsic and Atmospherically Forced Variability of the AMOC: Insights from a Large-Ensemble Ocean Hindcast. *Journal of Climate*, 2018, 31 (3), pp.1183-1203. 10.1175/JCLI-D-17-0168.1 . hal-03003510

HAL Id: hal-03003510

<https://hal.science/hal-03003510>

Submitted on 17 Nov 2021

HAL is a multi-disciplinary open access archive for the deposit and dissemination of scientific research documents, whether they are published or not. The documents may come from teaching and research institutions in France or abroad, or from public or private research centers.

L'archive ouverte pluridisciplinaire **HAL**, est destinée au dépôt et à la diffusion de documents scientifiques de niveau recherche, publiés ou non, émanant des établissements d'enseignement et de recherche français ou étrangers, des laboratoires publics ou privés.



Distributed under a Creative Commons Attribution 4.0 International License

Intrinsic and Atmospherically Forced Variability of the AMOC: Insights from a Large-Ensemble Ocean Hindcast

STEPHANIE LEROUX,^{a,b} THIERRY PENDUFF,^a LAURENT BESSIÈRES,^c JEAN-MARC MOLINES,^a
JEAN-MICHEL BRANKART,^a GUILLAUME SÉRAZIN,^d BERNARD BARNIER,^a
AND LAURENT TERRAY^c

^a *Université Grenoble Alpes, CNRS, IRD, Grenoble-INP, IGE, Grenoble, France*

^b *Ocean Next, Grenoble, France*

^c *CNRS/CERFACS, CECI UMR 5318, Toulouse, France*

^d *LEGOS, Université de Toulouse, IRD, CNES, CNRS, UPS, Toulouse, France*

(Manuscript received 15 March 2017, in final form 24 October 2017)

ABSTRACT

This study investigates the origin and features of interannual–decadal Atlantic meridional overturning circulation (AMOC) variability from several ocean simulations, including a large (50 member) ensemble of global, eddy-permitting ($1/4^\circ$) ocean–sea ice hindcasts. After an initial stochastic perturbation, each member is driven by the same realistic atmospheric forcing over 1960–2015. The magnitude, spatiotemporal scales, and patterns of both the atmospherically forced and intrinsic–chaotic interannual AMOC variability are then characterized from the ensemble mean and ensemble spread, respectively. The analysis of the ensemble-mean variability shows that the AMOC fluctuations north of 40°N are largely driven by the atmospheric variability, which forces meridionally coherent fluctuations reaching decadal time scales. The amplitude of the intrinsic interannual AMOC variability never exceeds the atmospherically forced contribution in the Atlantic basin, but it reaches up to 100% of the latter around 35°S and 60% in the Northern Hemisphere midlatitudes. The intrinsic AMOC variability exhibits a large-scale meridional coherence, especially south of 25°N . An EOF analysis over the basin shows two large-scale leading modes that together explain 60% of the interannual intrinsic variability. The first mode is likely excited by intrinsic oceanic processes at the southern end of the basin and affects latitudes up to 40°N ; the second mode is mostly restricted to, and excited within, the Northern Hemisphere midlatitudes. These features of the intrinsic, chaotic variability (intensity, patterns, and random phase) are barely sensitive to the atmospheric evolution, and they strongly resemble the “pure intrinsic” interannual AMOC variability that emerges in climatological simulations under repeated seasonal-cycle forcing. These results raise questions about the attribution of observed and simulated AMOC signals and about the possible impact of intrinsic signals on the atmosphere.

1. Introduction

a. Motivation and background

The Atlantic meridional overturning circulation (AMOC), as defined by the zonally integrated northward volume transport cumulated in the vertical in the Atlantic Ocean, plays a crucial role in the Earth’s climate system in redistributing heat within the ocean and connecting the Southern and Northern Hemispheres. The importance of AMOC for Earth’s climate has motivated numerous studies to investigate AMOC characteristics, dynamics,

and variability (e.g., review article by [Buckley and Marshall 2016](#)). Observational initiatives have also been implemented, or are planned to be, to achieve a long-term monitoring of the AMOC at different locations; these include the RAPID–MOCHA observational program started in 2004 at 26.5°N (e.g. [Hirschi et al. 2003](#); [Smeed et al. 2014](#)), the Observatoire de la Variabilité Interannuelle et Décennale (OVIDE) program in the Subpolar Gyre since 2002 ([Lherminier et al. 2007](#)) followed by the Overturning in the Subpolar North Atlantic Project (OSNAP) program since 2014 ([Lozier et al. 2017](#)), and the South Atlantic Meridional Overturning Circulation (SAMOC) international initiative at 34.5°S ([Garzoli et al. 2012](#)).

AMOC variability is linked to sea surface temperature (SST) and atmospheric variability through complex

Corresponding author: Stephanie Leroux, stephanie.leroux@ocean-next.fr

interactions over a wide spectrum of time scales (e.g., Buckley and Marshall 2016; Ducheze et al. 2016). For example, the AMOC accounts for a northward cross-equatorial ocean heat transport of approximately 0.4 PW, leading to heat convergence in the North Atlantic, and the amount of this hemispheric asymmetry sets the off-equatorial shift of the annual-mean location of the ITCZ in the atmosphere (e.g., Frierson et al. 2013; Marshall et al. 2014). On decadal time scales, the AMOC is seen as the main driver of the basinwide SST mode in the North Atlantic (referred to as the Atlantic multidecadal variability or oscillation; e.g., Kerr 2000; Deser et al. 2010), which plays an important role in regional climate by driving, for example, large-scale precipitation changes over the Sahel and the southern United States (e.g., Ting et al. 2009; Enfield et al. 2001).

The relative role of atmospheric forcing versus ocean internal processes in causing AMOC fluctuations, and the nature of the mechanisms at play, are not fully understood (e.g., Roberts et al. 2013a; Hirschi et al. 2013). On subannual time scales, AMOC variability is often seen as a passive response to local surface wind changes (e.g., Xu et al. 2014). In contrast, decadal AMOC variability is more coherent in latitude and is thought to be driven mainly by convection and water mass formation in the Labrador Sea (e.g., Yeager and Danabasoglu 2014; Roberts et al. 2013b). In addition, regional and local atmospheric conditions related to the phase of the North Atlantic Oscillation (NAO) or the amplitude of atmospheric high-frequency white noise can also excite or modulate AMOC variability (e.g., Danabasoglu 2008). It is, however, unclear how much of the AMOC variability is actually determined by the atmospheric forcing, relative to the contribution from ocean intrinsic processes (e.g., Hirschi et al. 2013; Buckley et al. 2012).

Penduff et al. (2011, 2014), Roberts et al. (2013a), and Hirschi et al. (2013) have raised the question of the role of mesoscale ocean eddies and how much they potentially contribute to interannual ocean variability in eddy-permitting OGCMs. Previous idealized modeling studies based on simplified ocean configurations forced with time-independent surface winds, or high-frequency noise, indeed predict that the AMOC might vary spontaneously up to low frequency (interannual–decadal time scales), even if those time scales are not present in the external forcing, just owing to the chaotic nature of the turbulent ocean system (e.g., Sévellec and Huck 2015; Dijkstra and Ghil 2005). However, the measure of this spontaneous, intrinsic, and chaotic source of AMOC low-frequency variability, relative to that induced by the atmospheric forcing, remains poorly known in a more realistic context, such as simulated by eddy-permitting OGCMs. This is the question we address

in the present study. It is an important aspect to better understand and quantify, given that most of the coupled atmosphere–ocean GCMs used for CMIP-type long-term climate projections up to now have used ocean components in the laminar regime (i.e., noneddying resolutions of about 1° – 2°). Those might, in fact, have underestimated ocean variability, and in particular AMOC variability, on all time scales, including interannual and decadal time scales. For instance, Sérazin et al. (2016) have shown that CMIP5 coupled models are likely underestimating sea level variability on decadal time scales in several regions in the midlatitudes. As eddy-permitting OGCMs are now progressively replacing their laminar counterparts for the future CMIP-type projections, studying ocean-only eddy-permitting experiments is essential in order to assess and quantify the influence of the ocean mesoscale on low-frequency variability (interannual and longer time scales), before those eddy-permitting configurations are incorporated in the future atmosphere–ocean coupled modeling systems [e.g., High Resolution Model Intercomparison Project (High-ResMIP); Haarsma et al. 2016]. A better quantification of the uncertainty associated with intrinsic variability for a given ocean variable, as a function of time scale and space, would also be useful information to provide to data assimilation systems or monitoring systems and to compare in magnitude to the other types of uncertainties introduced by, for example, the assimilated observations and the atmospheric forcing dataset.

A few recent studies based on eddy-permitting OGCMs have proposed different approaches to investigate the role of mesoscale eddies on low-frequency ocean variability. Hirschi et al. (2013) have compared twin experiments at eddy-permitting ($1/4^{\circ}$) and non-eddy (1°) resolution, consisting of a pair of 40-yr global ocean hindcasts at each resolution forced by the exact same surface fluxes and started with different initial conditions. They show that on subannual–interannual time scales, a large fraction of AMOC variability is induced and determined by the surface forcing, but in the eddy-permitting case, some of the variability is also clearly dependent on the initial conditions. From the spread between the two members of the eddy-permitting pair, they provide a first estimation of the intrinsic contribution to be up to approximately 30% of the total subannual–interannual AMOC variability. In the same idea, Roberts et al. (2013a) used an eight-member initial-condition ensemble of global ocean hindcasts to investigate the origins of the large transient weakening of the AMOC recorded in 2009/10 by the RAPID monitoring array at 26.5° N. Their model results show that the atmosphere played a dominant role in driving this recent interannual fluctuation.

The intrinsic low-frequency contribution to ocean variability has been quantified and characterized further in works by Penduff et al. (2011, 2014), Sérazin et al. (2015), and Grégorio et al. (2015). To isolate the intrinsic part of the ocean variability, they used 327-yr climatological global ocean simulations forced with atmospheric boundary conditions bearing no variability other than a climatological seasonal cycle identically repeated from year to year. Comparing noneddying (2°) and eddy-permitting ($1/4^\circ$ and $1/12^\circ$) versions of such climatological simulations, Grégorio et al. (2015) showed that in the eddying configurations only, a substantial part of the AMOC variability spontaneously emerges from the turbulent ocean under climatological atmospheric forcing. The noneddying simulation remains devoid of interannual variability. They also demonstrate that this intrinsic variability in the eddy-permitting case is of chaotic nature, intermittent in time, and widely spreads in time from months to multidecadal time scales.

b. Objectives, proposed approach, and outline

Building on the results from Grégorio et al. (2015), the present study takes a step further and investigates now the contribution of both intrinsic and forced AMOC variability in a global eddy-permitting ocean model under realistic atmospheric forcing (i.e., a forcing varying on all time scales). A large-ensemble modeling approach is followed as part of the Ocean Chaos–Impacts, Structures, Predictability (OCCIPUT) project (<http://meom-group.github.io/projects/occiput/>; Penduff et al. 2014; Bessières et al. 2017) in order to simulate simultaneously both contributions (intrinsic and forced) and subsequently separate them from one another via ensemble statistics. An ensemble of $N = 50$ members multiplied by 56-yr global ocean–sea ice hindcasts was thus performed, where all the members are driven by the same atmospheric forcing derived from atmospheric reanalysis datasets and started from perturbed initial conditions.

In this modeling framework, the ensemble mean can be taken as an estimate of the forced, deterministic variability, induced by the atmospheric boundary conditions shared by all the members. The spread about the ensemble mean, as measured by the ensemble standard deviation, or the ensemble probability density function (PDF), gives an estimate of the intrinsic, chaotic variability generated by the turbulent ocean at eddy-permitting resolution. For the sake of brevity and clarity in the following, we will mostly use the adjectives “intrinsic” and “forced” to qualify those two contributions to AMOC variability. What

we mean by this terminology is 1) the part of AMOC variability intrinsically emerging from the turbulent ocean at eddy-permitting resolution, owing to the chaotic nature of the system and thus sensitive to initial conditions (i.e., phase and amplitude varying from one member to another), and 2) the part of AMOC variability induced and phase-locked by the time-varying atmospheric forcing, deterministic in the sense that it is not sensitive to initial conditions and is shared identically by all the ensemble members.

Ensemble modeling is a commonly used approach in atmospheric and climate studies, but it has been much more rarely applied to eddy-permitting OGCM studies up to now, given the high computing cost of ocean models at this resolution. Previous studies on intrinsic AMOC variability with realistic ocean models have often been limited to one long simulation, to ensembles of small size [e.g., $N = 2$ in Hirschi et al. (2013) and $N = 8$ in Roberts et al. (2013a)], or to regional modeling [e.g., in the Agulhas region, with $N = 2$ in Biastoch et al. (2008)].

The main objective of this ensemble-based study is to provide a characterization and quantification of the AMOC variability that spontaneously arises in an eddy-permitting OGCM driven by a realistic forcing (i.e., varying on all time scales), and to compare it with the AMOC variability that is directly driven by the atmospheric variability. Compared to approaches based on climatological simulations (e.g., Grégorio et al. 2015), the ensemble strategy allows us to simulate simultaneously both the intrinsic and forced variability under a realistic, time-varying atmospheric forcing at all resolved time scales, and to subsequently separate them from one another for analysis. The interannual forced variability is, by design, excluded from climatological simulations whose forcing is devoid of any period longer than one year. The ensemble approach also allows us to extract the amplitude of the intrinsic variability as a function of time, to compare it with the atmospherically forced variability, and to investigate potential interactions between the two. It is then possible to assess whether the time-varying atmospheric forcing possibly modulates, damps, or paces the intrinsic AMOC variability, in comparison with what we may call the “pure intrinsic” variability isolated in a climatological simulation.

Section 2 describes the OCCIPUT ensemble, the model configuration, and the methodology details. Section 3 quantifies and discusses the relative proportion of intrinsic and forced AMOC variability deduced from the global ensemble. Section 4 investigates further the preferred time scales and spatiotemporal structures of the intrinsic contribution. Final conclusions are given in section 5.

TABLE 1. Model setups and simulations.

Simulation	ENSx50-occi025	ENSx10-natl025	CLIM-occi025	CLIM-Greg025
Domain	Global	North Atlantic (21°S–81°N)	Global	Global
Lateral conditions	—	Solid wall to Levitus monthly climatology with 28-gridpoint buffer.	—	—
Type	Ensemble hindcast	Ensemble hindcast	Climatology	Climatology
No. of members N	50	10	1	1
Time period	1960–2015	1993–2012	330 yr	327 yr
NEMO version	3.5	3.5	3.5	3.4
Resolution	1/4° and 75 vertical levels	1/4° and 46 vertical levels	1/4° and 75 vertical levels	1/4° and 46 vertical levels
Atm forcing set	DFS5.2 (all time scales)	DFS5.2 (all time scales)	Climatology from DFS5.2	Climatology from DFS4
Reference	Bessières et al. (2017)	Bessières et al. (2017)	Bessières et al. (2017)	Grégorio et al. (2015)

2. Modeling and methodology details

a. The global OCCIPUT ensemble simulation

The general concept and motivations for a fully probabilistic approach of ocean modeling are presented in Penduff et al. (2014) and Bessières et al. (2017). The latter study also presents the technical implementation and performances of this novel ensemble configuration of the NEMO modeling system (<http://www.nemo-ocean.eu>; Madec 2012).

The main OCCIPUT ensemble is made of 50 global ocean–sea ice hindcasts in the eddying regime, run for 56 years (1960–2015). The configuration is based on version 3.5 of NEMO, using a 1/4° eddy-permitting horizontal resolution (~27 km at the equator, decreasing poleward) and 75 vertical levels. It is forced by atmospheric conditions from the DRAKKAR forcing set DFS5.2 (Dussin et al. 2016), based on the reanalyses ERA-40 and ERA-Interim. The model characteristics and parameters (Table 1) are similar to those commonly used in the DRAKKAR-ORCA025 one-member setups (e.g., Barnier et al. 2006). They are also close to the parameters used for the 327-yr one-member climatological simulation studied in Grégorio et al. (2015).

The OCCIPUT ensemble run starts from a 21-yr, one-member spinup simulation performed in three successive phases:

- 1) The model is started from rest on 1 January 1958 and is driven for 18 years by the 6-hourly DFS5.2 forcing until 31 December 1976.
- 2) In January 1977, the spinup simulation is then driven by a modified forcing; over this month, all DFS5.2 forcing components are linearly transitioned from their state on 1 January 1977 to their state on 31 January 1958.
- 3) The standard DFS5.2 forcing is applied again for another 23 months between 1 February 1958 and 31 December 1959.

This strategy yields a 21-yr spinup phase (from 1958 to 1976, then from 1958 to 1959) that includes a smooth

transition from January 1977 back to January 1958. This compromise allows us to maximize the duration of both the single-member spinup simulation and the ensemble hindcast, and to minimize the perturbation in the forcing during the transition because 1977 was found to be a reasonable analog of 1958 in terms of key climate indices (El Niño–Southern Oscillation, North Atlantic Oscillation, and southern annular mode).

Starting from this 21-yr spinup simulation, the 50 members of the OCCIPUT ensemble hindcast are then generated in 1960 by activating a small stochastic perturbation in the density equation of each member (see also Brankart et al. 2015; Bessières et al. 2017). This stochastic perturbation is only applied for the first year (1960) to seed the ensemble dispersion. It then remains switched off for the rest of the ensemble hindcast (from 1961 to 2015). Once the stochastic perturbation is stopped at the end of 1960, the 50 members are thus integrated from slightly perturbed initial conditions and forced by the same atmospheric conditions. The code is parallelized with a double-parallelization technique described in Bessières et al. (2017) so that the 50 members are integrated simultaneously through one single executable. Online ensemble statistics can thus be computed along the integration.

As explained in the following, our diagnostics are then mostly performed over the period 1979–2015, that is, after 19 years of integration of all the members in addition to the monomember spinup. The total effective spinup time of the ensemble simulation before most analyses is, therefore, 40 years.

b. Additional simulations

The results from the global ensemble hindcast (ENSx50-occi025) will be compared with three additional simulations, all summarized with their main characteristics in Table 1. We will investigate a one-member 330-yr climatological simulation (CLIM-occi025). It is similar to the climatological simulation by

Grégorio et al. (2015) (CLIM-Greg025), but it uses the same model configuration and parameters as the ensemble ENSx50-occi025 and is driven by a climatological atmospheric forcing derived from the same dataset (DFS5.2). The climatological forcing is, by construction, devoid of any other variability than the seasonal cycle, and CLIM-occi025 will provide a measure of the pure intrinsic variability, that is, simulated in the absence of interannually varying and synoptic forcing from the atmosphere. The amplitude and characteristics of the pure intrinsic variability will then be compared with their counterparts in the ensemble hindcast to assess the impact of the reanalyses forcing on the intrinsic variability. We will also present results from a North Atlantic regional ensemble hindcast from 1994 to 2012 with $N = 10$ members (ENSx10-natl025). Its southern lateral boundary is set at 20°S and is treated as a solid wall with a 28-gridpoint buffer zone where the ocean state is restored to monthly Levitus climatological conditions (Levitus et al. 1998). In this regional setup, the AMOC variability north of 20°S is thus isolated from any influence coming from the south. We will compare the regional and global ensembles to assess the potential origin of intrinsic AMOC variability in the Atlantic basin.

c. AMOC diagnostics

The AMOC is diagnosed as the zonally integrated northward volume transport cumulated in the vertical in the Atlantic basin from monthly mean model output. The annual AMOC dataset is then computed from the monthly mean output by applying a nonrunning 12-month averaging operator. We mostly show results based on the AMOC computed in density coordinates (AMOC_{σ_2}) with a reference depth at 2000 m, following Zhang and Delworth (2005) and Grégorio et al. (2015). Some comparison with the AMOC in geopotential coordinates (AMOC_Z) is provided in section 3f. At latitudes lower than about 35°N little difference is found in our results in density or geopotential coordinate systems.

We focus our analysis on the maximum value of the AMOC in the vertical, corresponding to the total northward volume transport (i.e., the AMOC upper branch). The search for the maximum transport is conducted for waters denser than 35.5 kg m^{-3} (AMOC_{σ_2}) or below 500 m (AMOC_Z) to avoid any locally shallower extremum.

Unless mentioned otherwise, AMOC variability is computed from the anomaly time series after applying a nonparametric locally estimated scatterplot smoothing (LOESS) operator on each ensemble member that removes the long-term nonlinear trend and time mean (LOESS detrending; Cleveland and Devlin 1988). Only

the time scales fully resolved within the length of the examined time segment are thereby retained. In other words, when detrending the entire 56-yr simulation, we discard the time mean and the very low-frequency variability of periods T longer than the duration of the simulation, and we also discard any potential long-term trends that might correspond to some long-term climate forcing and to the model drift. The effect of this detrending operator is illustrated in section 3a.

d. Definitions and notations

We now introduce some notations and definitions related to how we quantify the intrinsic and forced contributions of AMOC variability. We define $f_i(t, \phi)$ as the total AMOC_{σ_2} anomaly time series at a given latitude ϕ after nonlinear detrending, where t stands for the time (yr) and i is the index of the ensemble member. We use overbars for the time-mean operator and angled brackets for the ensemble-mean operator. The function $f_i(t)$ can be decomposed as

$$f_i(t) = \langle f_i(t) \rangle + f'_i(t), \quad (1)$$

where $\langle f_i \rangle$ is the ensemble mean (i.e., the forced component), and parameters f'_i are the $N = 50$ intrinsic components. Note that because the $N = 50$ total anomaly signals $f_i(t)$ have each been nonlinearly detrended and thus cleaned of their mean and unresolved very low frequencies, we also have $\overline{f_i(t)} \sim 0$ and $\langle \overline{f_i(t)} \rangle \sim 0$ for each member i .

We define σ^2 as the time-variance operator. Applied to the ensemble mean, it gives

$$\sigma^2_{\langle f \rangle} = \frac{1}{T-1} \sum_{t=1}^T [\langle f_i(t) \rangle - \overline{\langle f_i(t) \rangle}]^2. \quad (2)$$

We define ε^2 as the ensemble-variance operator. Applied to $f'_i(t)$, it gives

$$\varepsilon^2(t) = \frac{1}{N-1} \sum_{i=1}^N f'^2_i(t). \quad (3)$$

In this study, we will hereafter quantify and discuss the amplitude of the intrinsic and the forced AMOC variabilities, and their relative contributions, with the amplitude ratio R :

$$R = \frac{A_{\text{intrinsic}}}{A_{\text{forced}}}, \quad (4)$$

where $A_{\text{intrinsic}}$ is our time-independent estimate for the amplitude of the intrinsic variability:

$$A_{\text{intrinsic}} = \sqrt{\overline{\varepsilon^2}}, \quad (5)$$

and A_{forced} is our time-independent estimate for the amplitude of the forced variability:

$$A_{\text{forced}} = \sigma_{(f)}. \quad (6)$$

We also define $A_{\text{tot},i}$ as our estimate for the amplitude of the total variability in each member i as

$$A_{\text{tot},i} = \sigma_{f_i}. \quad (7)$$

These three amplitudes, $A_{\text{intrinsic}}$, A_{forced} , and $A_{\text{tot},i}$ as defined above, are linked to each other by the sum of their squared values (variances):

$$A_{\text{intrinsic}}^2 + A_{\text{forced}}^2 = \overline{\varepsilon^2} + \sigma_{(f)}^2 = \langle \sigma_{f_i}^2 \rangle \quad (8)$$

$$= \langle A_{\text{tot},i}^2 \rangle. \quad (9)$$

In the following sections, we mostly discuss the amplitude of the AMOC fluctuations (in Sverdrups; $1 \text{ Sv} \equiv 10^6 \text{ m}^3 \text{ s}^{-1}$), but note that we rather plot the associated variances (Sv^2) to conserve additivity properties in the figures. We therefore provide two different axes in the related figures in order to facilitate the direct reading of both variance and amplitude values from the plots.

3. Estimates of intrinsic and forced interannual AMOC variability

In this section, we first illustrate our ensemble approach at two key locations in the Atlantic basin: 26.5°N and 34.5°S . The former latitude is that of the observational RAPID–MOCHA array monitoring the AMOC since 2004. The latter latitude is targeted by the SAMOC international initiative for a project monitoring the South Atlantic meridional overturning circulation, where the dynamics of the AMOC is known to be influenced by the Agulhas Current leakage (e.g., [Ansorge et al. 2014](#); [Garzoli et al. 2012](#)). We then extend some diagnostics to all latitudes.

a. Centered AMOC time series at 26.5°N and 34.5°S

[Figures 1a and 1b](#) present the annual-mean AMOC_{σ_2} anomaly time series from ENSx50-occi025 and CLIM-occi025, respectively, before applying the detrending operator. The time series are here simply centered in time by removing their individual time means (of which the distribution is given in [Figs. 1c, d](#) for reference). The anomaly time series illustrate the two types of variability that we are going to quantify and compare in this study:

- Some intermember spread is clearly seen across the 50 individual trajectories, thus confirming the sensitivity of our eddy-permitting OGCM to slightly perturbed initial conditions, up to low-frequency time scales (interannual and longer).
- At each latitude, the 50 time trajectories also share some similarities, such as the large increase of the AMOC in 1994 at 26.5°N , or the large drop in 2010 at both latitudes. These common fluctuations provide us with an estimate of the variability forced by the atmospheric surface conditions that is identically seen by each of the 50 members and thus captured in the ensemble mean. Both the 1994 and 2010 AMOC extrema are, indeed, attributed to atmospheric causes in the literature ([Zhao and Johns 2014](#); [Roberts et al. 2013a](#); [Reichler et al. 2012](#)). Note, however, that only the 2010 extremum extends over the two latitudes plotted here, suggesting that it might be related to a larger-scale forcing anomaly.

[Figure 1](#) also shows the long-term trends that are discarded in the rest of the study: a decreasing trend of about -3 Sv is seen in each ensemble member over the 56 years of simulation. Note that these trends are not necessarily linear: at 26.5°N , for example, they all decrease more steeply in the second half of the simulation, while this decrease is more linear over the same period at 34.5°S . A long-term trend also affects the climatological simulation CLIM-occi025. These nonlinear trends include the combined effects of the long-term climate forcing as well as the model drift. The differences in ENSx50-occi025 and CLIM-occi025 trends come from the very low-frequency variability, possibly forced by the atmosphere in ENSx50-occi025 and/or generated from intrinsic processes in both simulations. In any case, this very low-frequency contribution is not fully resolved within our 56-yr simulation and will thus be discarded in the following by applying the nonlinear detrending operator to each ensemble member.

This very low-frequency AMOC variability is not necessary negligible but must be discarded to ensure that the subsequent analyses are focused on a clear and well-resolved range of time scales (from interannual to decadal). This frequency restriction in particular is required to compare the amplitude of the intrinsic and forced variability over the same spectral window: A_{forced} is estimated from a time variance and would be influenced by nonlinear trends without this preprocessing, while $A_{\text{intrinsic}}$, estimated from an ensemble variance, would not.

Our estimation of the intrinsic variability $A_{\text{intrinsic}}$ is thus a conservative estimation because it does not

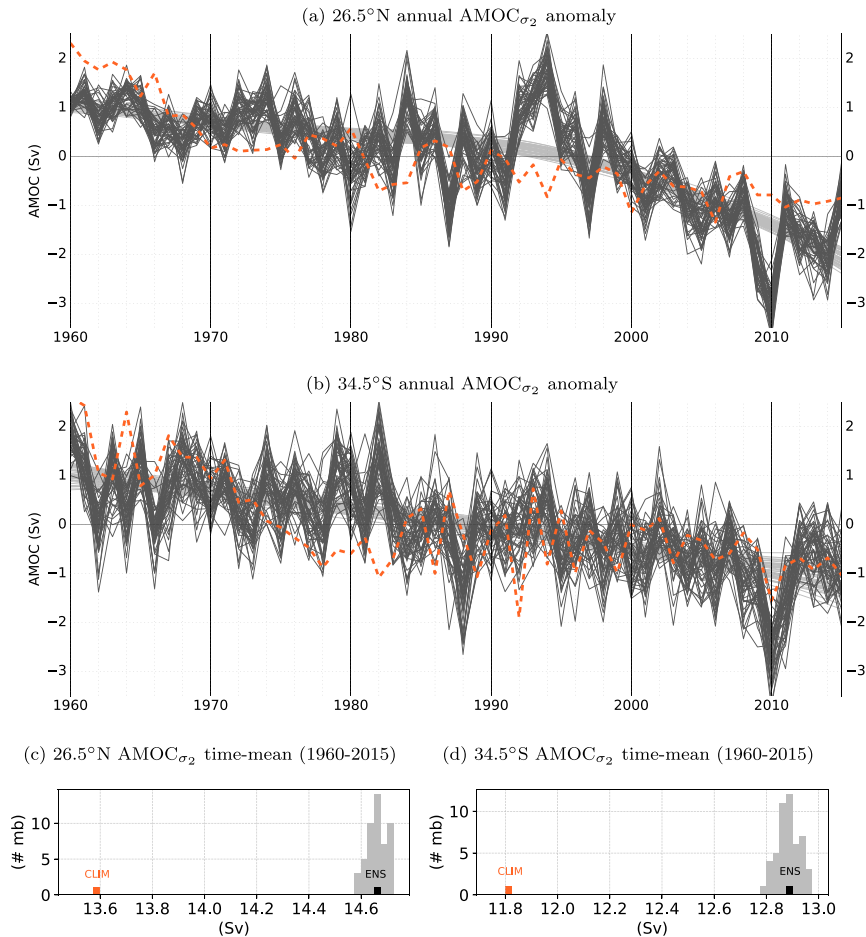


FIG. 1. Annual-mean $AMOC_{\sigma_2}$ anomaly time series at (a) 26.5°N and (b) 34.5°S from the ensemble ENSx50-occi025 (black) and CLIM-occi025 (dashed orange) before applying the detrending operator. The time series are simply centered in time by removing their individual time means. The nonlinear trends computed from the LOESS method for each of the members are also shown in light gray in the background. The distribution of the removed time-mean values is shown at (c) 26.5°N and (d) 34.5°S for ENSx50-occi025 (individual time means in gray and time mean of the ensemble mean in black) and for CLIM-occi025 (orange).

include longer multidecadal time scales that were detected under seasonal forcing (Grégorio et al. 2015).

b. Detrended AMOC time series at 26.5°N and 34.5°S

To quantify the relative contribution of intrinsic and atmospherically forced variability, we now focus on the detrended annual $AMOC_{\sigma_2}$ time series in Figs. 2 and 3. The ensemble spread, defined as $\varepsilon^2(t)$ in section 2, is plotted as a function of time in Figs. 2b and 3b. At both latitudes, it undergoes an initial growth phase in the first few years, after which it stabilizes: on average, over 1979–2015, we measure $A_{\text{intrinsic}} = 0.36$ Sv at 26.5°N and 0.53 Sv at 34.5°S. The amplitude $\varepsilon^2(t)$ of the intrinsic variability slightly fluctuates from year to year around its mean value. But these fluctuations cannot be held as significant here because they lie within the 95% confidence interval

associated with the successive computations of the ε^2 estimate, each year, from our finite-size samples (see Figs. 2b and 3b and the appendix for details). Assessing whether the ensemble spread $\varepsilon^2(t)$ actually varies in time for physical reasons would require a narrower confidence interval (i.e., a larger ensemble run).

It has also been verified from an additional experiment (not shown here) that the level of $A_{\text{intrinsic}}$ does not significantly change when the small stochastic perturbation is activated permanently for eight years of simulation instead of being stopped after the first year as in ENSx50-occi025 and ENSx10-natl025. In those simulations, the 1-yr stochastic perturbation only aims to seed the initial dispersion of the members. The intrinsic variability is thereafter fully controlled by nonlinear ocean dynamics.

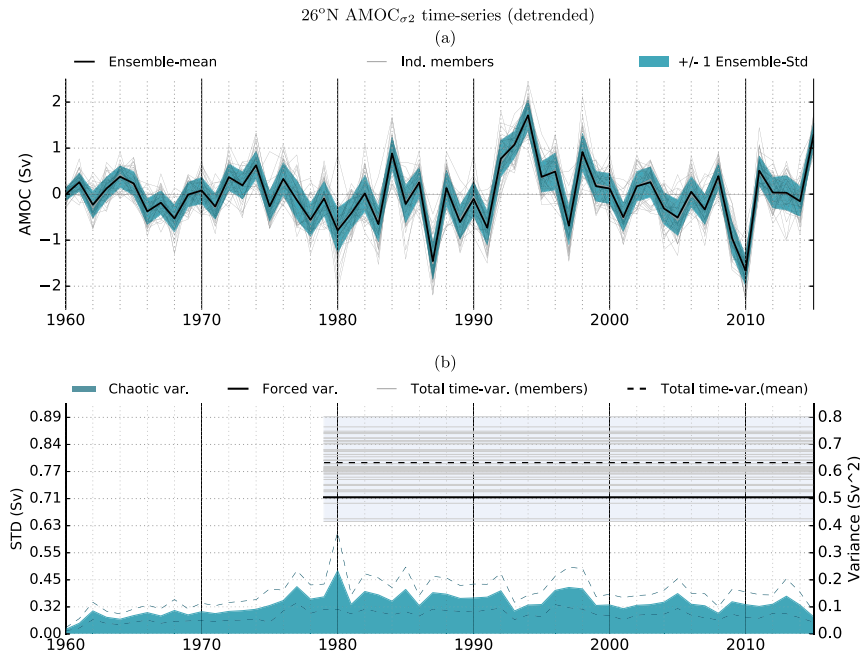


FIG. 2. (a) Time series of the annual-mean $AMOC_{\sigma_2}$ anomalies at 26°N from ENSx50-occi025 after nonlinear (LOESS) detrending. The 50 individual trajectories are shown with the thin gray lines; the ensemble mean is shown with the thick black line; and the interval $\pm \epsilon(t)$ is shaded. (b) Ensemble and time statistics: the ensemble variance $\epsilon^2(t)$ (intrinsic variability; blue shading) is compared with A_{forced}^2 , the time variance of the ensemble mean (i.e., the forced variability; thick black line). The 95% confidence interval, when taking into account the error made on ϵ^2 due to the finite size of the ensemble, is shown with the thin dashed blue-green lines (see the appendix for details). Thin solid gray lines show the distribution of $A_{\text{tot},i}^2$, the total time variance from the 50 members. Its mean value $\langle A_{\text{tot},i}^2 \rangle$ is shown with the thick dashed black line. Note that tick marks are provided on a square root scale on the left y axis in order to read more easily the standard deviation values (Sv) corresponding to the plotted variances. Tick marks on a linear scale are on the right y axis to read the variances (Sv^2).

The amount of intrinsic variability ($A_{\text{intrinsic}}$) at both latitudes can now be compared to the amount of atmospherically forced variability (A_{forced}) in Figs. 2b and 3b. We find that the intrinsic contribution is substantial, reaching the same order of magnitude as the atmospherically forced contribution at 34.5°S ($R = 97\%$) and half that at 26.5°N ($R = 51\%$). Note that for this comparison we restrict the time statistics to the period 1979–2015 to ensure that the forcing dataset DFS5.2 is fully varying on interannual time scales. In the pre-1979 period, DFS5.2 precipitation and radiative fluxes are, indeed, devoid of interannual variability, which might lead to an underestimation of the atmospherically forced AMOC variability (see Dussin et al. 2016).

In accordance with the substantial amount of intrinsic variability detected at these latitudes, the total time variability $A_{\text{tot},i}$ also varies significantly from one member to another (plotted in thin light gray lines in Figs. 2b and 3b). In other words, the ensemble approach provides us here with an estimate of the uncertainty usually associated

with the AMOC time variability on interannual time scales when the latter is computed from just a single eddy-permitting simulation. We are able to quantify how much this time variability might differ between two simulations due solely to the sensitivity to initial conditions: at 34.5°S , the ensemble-mean value of the total time variability ($\langle A_{\text{tot}} \rangle$, thick dashed line) is about 0.75 Sv, but individual $A_{\text{tot},i}$ values can differ from one member i to another by up to 0.3 Sv (from minimum to maximum). At 26.5°N , $\langle A_{\text{tot}} \rangle$ is about 0.8 Sv and can differ from one member to another by up to 0.25 Sv (from minimum to maximum). Note also that the total variability $A_{\text{tot},i}$ from some individual members can be smaller than the forced variability A_{forced} (Fig. 2b). This can happen in cases where the intrinsic and forced time signals [$f_i'(t)$ and $\langle f(t) \rangle$, respectively] cancel out each other in part resulting from anticorrelation of their respective phases: the phase of $\langle f(t) \rangle$ is fixed and determined by the atmospheric forcing, but the phase of each of the 50 $f_i'(t)$ is random and differs from one member to another.

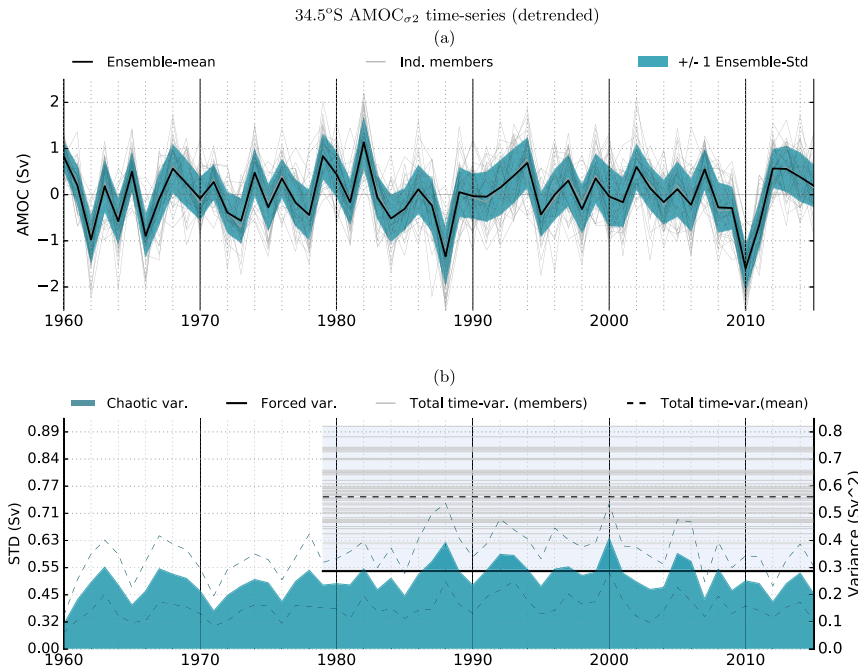


FIG. 3. As in Fig. 2, but at 34.5°S.

c. Meridional distribution of intrinsic and forced AMOC variability

The diagnostics for the intrinsic, forced, and total variability ($A_{\text{intrinsic}}^2$, A_{forced}^2 , and $A_{\text{total},i}^2$) are now applied to all latitudes in Fig. 4a. We find that the forced variability dominates the intrinsic variability in the entire basin, but the intrinsic variability reaches a substantial level in several regions. The amplitude of the intrinsic variability $A_{\text{intrinsic}}$ gradually increases from north to south, from about 0.1 to 0.5 Sv in amplitude, with two additional local peaks at 0.4 Sv around 24° and 37°N. The northern peak is collocated with the mesoscale-active region associated with the Gulf Stream separation.

In contrast, the atmospherically forced variability shows two highs of about 0.95 Sv around 15° and 45°N and reaches minima at both the northern and southern ends of the basin. As a result, the amplitude ratio R between the intrinsic and forced variability (Fig. 4b) is the largest in the South Atlantic around 35°S with a ratio of 100%, and around 24° and 37°N with a ratio of $R = 60\%$, collocated with the $A_{\text{intrinsic}}$ maxima. Even in the less active regions, we find a minimum amplitude ratio of about 25% (in the northern tropics and in the subpolar region). Our results are in good agreement with the ratio estimated in the precursor study by Hirschi et al. (2013) from a pair of simulations ($N = 2$) at the same resolution and for interannual time scales in the Atlantic basin (cf. their Fig. 14c). Note also that

both the RAPID and the SAMOC projects are located at latitudes where the relative influence of the intrinsic ocean “noise” on interannual AMOC variability reaches its highest values in the Atlantic basin (respectively, with half and with same orders of magnitude as the forced variability). More generally, our results advocate for taking better into account this type of “intrinsic uncertainty” when comparing observed AMOC records to eddy-permitting model simulations, and so even on low-frequency time scales. The higher the level of intrinsic low-frequency noise at a given latitude, the smaller the chance that the correlation can be high between a given simulation and the observational record at this latitude. This implication is further developed in the next paragraph.

d. Comparison with the observations at the RAPID array

We present the comparison of the ensemble with the observational record at the RAPID array (26.5°N) in the form of Taylor-type diagrams (Taylor 2001) in Fig. 5. This type of representation is useful to summarize time statistics (time standard deviation and correlation) and to compare each member of a simulated ensemble with a single observed time series. Time statistics are computed over the common available period between the two, that is, 2004–15. The first diagram (Fig. 5a) compares the annual AMOC time series of each ensemble member

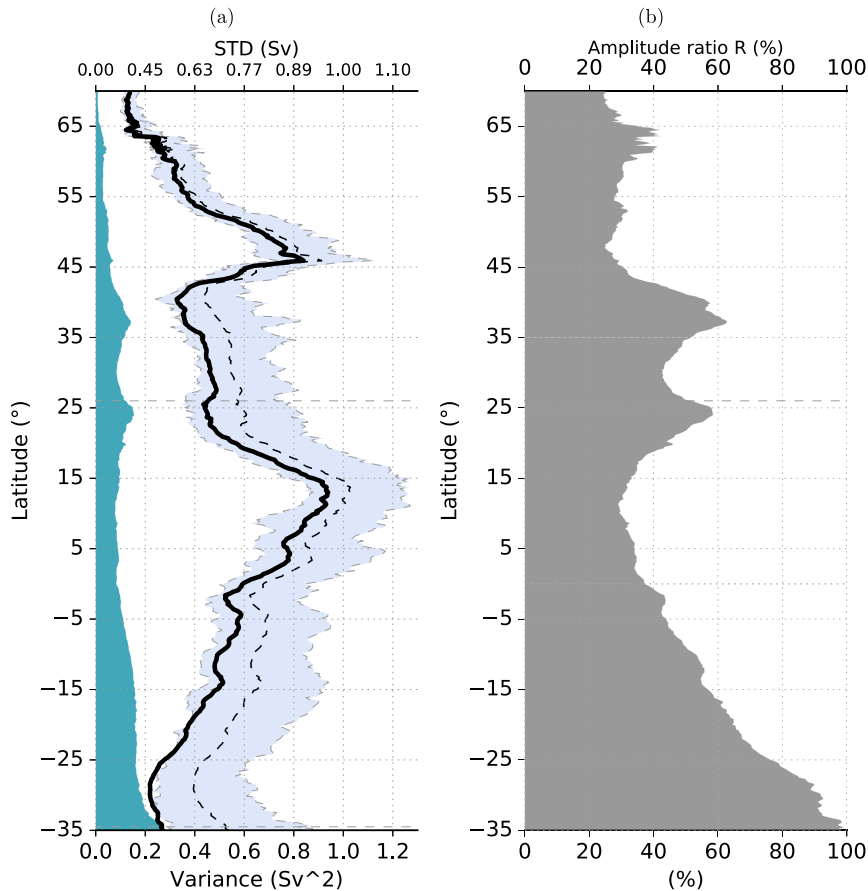


FIG. 4. (a) Intrinsic and forced components of interannual AMOC_{σ_2} variance ($A_{\text{intrinsic}}^2$ in blue shading and A_{forced}^2 in thick black line, respectively) as a function of latitude from ENSx50-occi025, detrended, over 1979–2015. The distribution of the total temporal variability in each member is shown with dashed lines [$\min(A_{\text{tot},i}^2)$, $\langle A_{\text{tot},i}^2 \rangle$, and $\max(A_{\text{tot},i}^2)$] and light blue shading. Note that tick marks are provided on a square root scale on the top x axis in order to read more easily the standard deviation values corresponding to the plotted variances. Tick marks on a linear scale are on the bottom x axis. (b) Amplitude ratio R of the intrinsic-to-forced components ($R = A_{\text{intrinsic}}/A_{\text{forced}}$; %) from ENSx50-occi025 as a function of latitude.

$[f_i(t)]$ to the observational record at the RAPID array, taken as the reference, over the common available period 2004–15. Consistent with many previous studies with forced ocean models (e.g., Roberts et al. 2013a), the members underestimate the total time variability compared to the observations (all the normalized members' time standard deviations are smaller than 1). But note that the member's standard deviation ratios range from 0.48 and 0.84 among the members as a consequence of sensitivity of the members' time statistics to initial conditions. Furthermore, the correlation between each of the members' time series and the observational record ranges from 0.38 to 0.85. For 11 of the 50 members, the correlation is not significant at the 95% level (using the Student's t test and Fisher's transform). Because the variability of the observational record includes an

intrinsic, random contribution as in any of the members, the correlation of the observations with the ensemble mean is higher than with most individual members. In other words, the higher the level of intrinsic noise in the time series, the less likely it is that the two time series will fluctuate with an identical phase.

The second Taylor diagram (Fig. 5b) presents an alternative view, following an approach proposed in previous literature (e.g., Shin and Sardeshmukh 2011). It provides additional information about the dispersion of the ensemble and its signal-to-noise ratio. The diagram is this time constructed using each of the 50 individual members' AMOC time series $f_i(t)$ successively taken as the reference, and comparing it to the 49 other members and to the RAPID observational time series. Consistent with Fig. 5a, we find that the correlation of a member

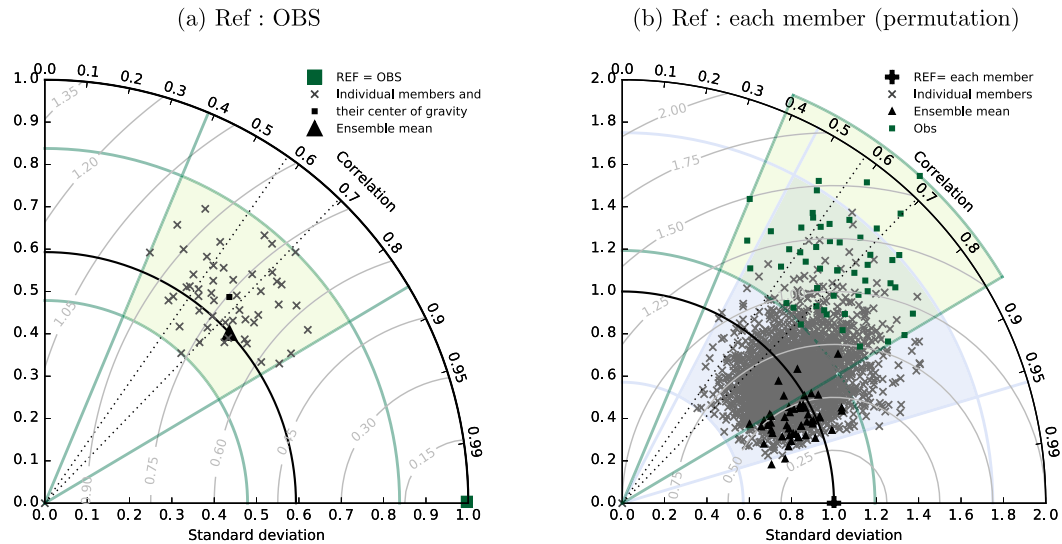


FIG. 5. (a) Taylor diagram (Taylor 2001) using the 2004–15 RAPID observational time series (annual means) as the reference. The RAPID time series is compared to the annual AMOC time series $f_i(t, \phi)$ of each ENSx50-occi025 individual member and to the ensemble-mean time series $\langle f(t, \phi) \rangle$ at $\phi = 26.5^\circ\text{N}$. For each point on the diagram, the angle with the horizontal axis shows the correlation with the reference time series, and the radial distance to the origin shows the ratio of their time standard deviations. In addition, the radial distance to the reference point corresponds to the RMS between the two time series (light gray arcs and labels). The green lines and shaded area mark out the minimum and maximum correlations and std dev values between the observational reference and the $N = 50$ members. The gray dotted lines indicate the significance threshold at the 95% and 99% levels for a Pearson correlation based on 19 years. (b) Taylor diagram permuting each member $f_i(t, \phi)$ alternatively as the reference. The diagram thus describes the correlation and std dev ratio between each member (at 26.5°N) and the 49 other members (gray crosses), the ensemble mean (black-filled triangles), and the observational record at the RAPID array (green-filled squares). The blue lines and blue-shaded area mark out the minimum and maximum correlation and std dev values between the members. The green lines and green shaded area mark out the minimum and maximum correlation and std dev values between the ensemble members and the observational record.

with the observational time series ranges from 0.38 to 0.85 (green shading). In addition, the diagram also shows that the correlation of a member with the other members ranges from 0.45 to 0.95 (blue shading). A situation where all intermember correlations are significantly higher than member-observation correlations would suggest underdispersion of the ensemble. This is not the case here because intermember correlations can be almost as low (0.47) as member-observation correlations (0.38 at the smallest). The opposite situation is not present here either because intermember correlations are not all smaller than member-observation correlations; such a case would have indicated a too-small signal-to-noise ratio in the model compared to the real world (i.e., overdispersion of the ensemble). This potential issue, or “signal-to-noise paradox,” had been pointed out in previous coupled climate simulations (e.g., Eade et al. 2014) but does not seem to affect our ensemble at this latitude.

e. On the location of intrinsic variability sources

Figure 6a now compares $A_{\text{intrinsic}}$ computed from the global ensemble (ENSx50-occi025) and from the North

Atlantic regional ensemble (ENSx10-natl025). Note that $A_{\text{intrinsic}}$ is this time computed in geopotential coordinates (from AMOC_Z) and over 1994–2012 only, as it was the common denominator in terms of model output availability for all the simulations compared in Fig. 6. We find that north of the equator, the amount of intrinsic variability is fairly similar in both the regional and global ensembles; the discrepancies remain everywhere within the range of the fluctuations from year to year in the global ensemble (shading in Fig. 6a). The amplitude of the intrinsic variability $A_{\text{intrinsic}}$ from the regional ensemble decreases south of the equator and logically reaches zero at the southern boundary, where all members are restored to monthly Levitus climatological conditions, yielding a damping of intrinsic variability. The similarity of $A_{\text{intrinsic}}$ in the regional and global ensembles to the north of the equator suggests that the intrinsic variability on these time scales might be generated within the North Atlantic region. In contrast, $A_{\text{intrinsic}}$ from the equator to 20°S is much lower in the regional than in the global ensemble, and it suggests another source of intrinsic variability located farther south than the southern boundary of the regional

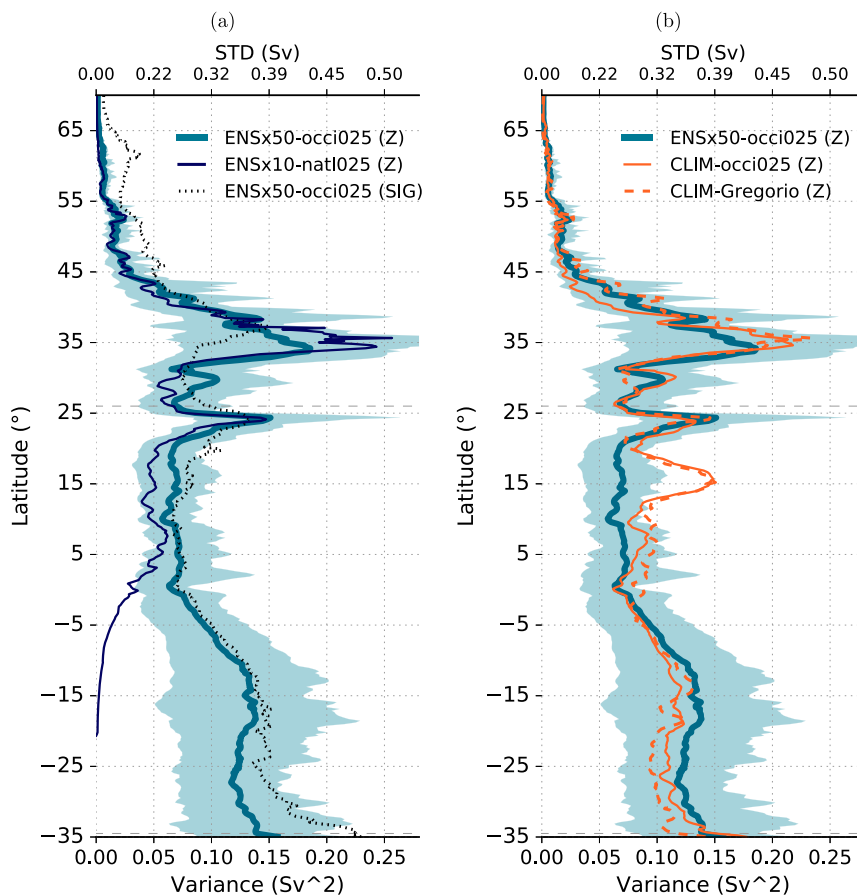


FIG. 6. Time-averaged intrinsic variance $A_{\text{intrinsic}}^2 = \overline{\varepsilon^2(t)}$ plotted as a function of latitude, computed in geopotential coordinates (from AMOC_Z) over 1994–2012 from (a) the global ensemble ENSx50-occi025 and the regional North Atlantic ensemble ENSx10-natl025 and (b) the global ensemble ENSx50-occi025 and the climatological simulations CLIM-occi025 and CLIM-Greg025. In (a), $A_{\text{intrinsic}}^2$ from ENSx50-occi025 is also shown in density coordinates for comparison. The fluctuations of $\varepsilon^2(t)$ from one year to another in ENSx50-occi025 are represented by a light shading between $\varepsilon^2(t)_{\text{min}}$ and $\varepsilon^2(t)_{\text{max}}$. Note that tick marks are provided on a square root scale in the top x axes in order to read more easily the standard deviation values corresponding to the plotted variances (tick marks on a linear scale in the bottom x axes).

run (20°S). This hypothesis is supported further by the results of the EOF analysis discussed in section 4.

f. Comparison between AMOC_{σ_2} and AMOC_z

The consistency of our results using the AMOC in either density coordinates or geopotential coordinates is also shown in Fig. 6a. South of 45°N, the latitudinal profiles are very consistent in both coordinate systems; everywhere the discrepancies remain within the range of the fluctuations from year to year (shading in Fig. 6a). The latitudinal profiles only differ significantly at higher northern latitudes, where the variability is small in both cases, but the value for AMOC_Z is only half the one obtained for AMOC_{σ_2} [which is consistent with previous studies such as Zhang and Delworth (2005) or Grégorio

et al. (2015)]. This weak intrinsic variability north of 45°N might be partly accounted for by the modest (1/4°) horizontal resolution of the model: the Rossby number is small in this latitude range, and turbulence is less well-resolved than at lower latitudes. The intrinsic AMOC variability was indeed shown by Grégorio et al. (2015) to be smaller at 1/4° than at 1/12° resolution in the subpolar region, while it is of fairly similar amplitude for both resolutions at lower latitude than about 40°N (cf. their Fig. 7b).

g. On the influence of atmospheric fluctuations on intrinsic AMOC variability

To what extent is the intrinsic AMOC variability sensitive to interannually varying atmospheric forcing, compared to

the pure intrinsic variability in the climatological simulations? To investigate this question, we now focus on $A_{\text{intrinsic}}$ from ENSx50-occi025 and from the two climatological simulations CLIM-occi025 and CLIM-Greg025 (Fig. 6b).

To compute the equivalent of an ensemble spread from each climatological simulation, we divide the 330 yr into 17 segments of 19 yr (same length as the 1994–2012 period considered here). Each of these time segments is processed and nonlinearly detrended in the same manner as any member of the “true” ensemble ENSx50-occi025 so that both ensembles include the same time-spectral content. Finally, a pseudo $\varepsilon(t)$ and a pseudo $A_{\text{intrinsic}}$ are computed from the ensemble spread between these 17 climatological segments.

We find that the latitudinal distributions of $A_{\text{intrinsic}}$ from CLIM-occi025 and from CLIM-Greg025 are remarkably similar, despite the differences in their model versions, resolutions, and setups (Table 1), giving good confidence in the consistency of our results with previous studies (Grégorio et al. 2015; Sérazin et al. 2015) and across NEMO configurations in general. We also find that $A_{\text{intrinsic}}$ from the climatological runs, which could be labeled as pure intrinsic variability, remains almost unchanged under realistic forcing (ENSx50-occi025). Overall, it means that the existence of low-frequency variability in the atmospheric forcing barely affects the amount and distribution of intrinsic variability in the simulation (as far as the AMOC is concerned, at least). In other words, we do not see any systematic effect of the atmospheric forcing to pace or lock the phase of the AMOC spontaneous fluctuations. Although a few notable differences appear locally, the main one being a peak of intrinsic variability around 15°N in the climatological runs, absent from the ensemble hindcast. This peak is the only occurrence where the climatological $A_{\text{intrinsic}}$ clearly exceeds the envelope of the year-to-year fluctuations of the hindcast $A_{\text{intrinsic}}$ (shading in Fig. 6b). A more detailed investigation is needed to elucidate the dynamical mechanism for this significant peak of intrinsic variability in the climatological runs. But note that according to Fig. 4, this latitude coincides with a maximum of forced variability, suggesting that at this location, the variability forced by the atmosphere might be locally able to damp or lock the phase of the intrinsic variability that otherwise develops randomly in the climatological runs at this location.

4. Spatiotemporal scales and structures of the intrinsic AMOC variability

a. Meridional distribution of preferred AMOC variability time scales

We now compare the spectral characteristics (time frequencies) of $A_{\text{intrinsic}}$ and A_{forced} as a function of

latitude in Fig. 7, based on AMOC_{σ_2} from the global ensemble ENSx50-occi025. To get a more accurate frequency resolution for this analysis, we directly use the monthly output (with the nonlinear trends removed as before). Figure 7a shows the power spectral density (PSD) computed from the ensemble mean at each latitude over the entire period 1960–2015. With the notation from section 2, it reads $\text{PSD}_{(f(t))}$. Figure 7b shows the average of the 50 individual PSDs computed from the intrinsic variability of each member [i.e., $\langle \text{PSD}_{f_i(t)} \rangle$]. A weak smoothing operator is also applied on each PSD in the frequency domain (convolution with a 9-point Hanning window), simply to reduce graphical noise, with no significant effect on the main spectrum characteristics or on the resulting integrated variance.

The spectral information in Fig. 7 is consistent with the latitudinal distribution of the variance in Fig. 4. The two maxima in A_{forced} seen around 45° and 10°–15°N in Fig. 4 coincide with the two main spectral peaks in Fig. 7a. Interestingly, the spectral analysis indicates that the maximum of forced variability at 45°N is associated mostly with decadal time scales, while the second peak of forced variability around 5°–15°N is associated with much shorter time scales in the interannual–subannual range. Note that the forced decadal peak centered on 45°N is consistent with the AMOC decadal fluctuations discussed in the literature in this region as driven by convection in the Labrador Sea, and indirectly by NAO activity (e.g., Böning et al. 2006; Bingham et al. 2007; Yeager and Danabasoglu 2014).

In addition, we find that the spectral characteristics of $A_{\text{intrinsic}}$ are substantially different from those of A_{forced} . The main peak in the distribution of $A_{\text{intrinsic}}$, located around 35°S, is associated with time scales in the interannual–subannual range. South of the equator, the power spectral density of $A_{\text{intrinsic}}$ increases gradually southward, mostly centered on short interannual time scales, but with substantial energy up to periods of 10 years and more.

Black contours in both panels of Fig. 7 show the ratio of the intrinsic and forced PSDs on a decibel (dB) scale [i.e., $R_{\text{PSD}} = 10\log_{10}(\text{PSD}_{\text{intrinsic}}/\text{PSD}_{\text{forced}})$]. Around 35°N, the intrinsic and forced variabilities are seen to be of similar magnitude ($R_{\text{PSD}} = 0$ dB; contours marking 100%) in the interannual and subannual range (T shorter than ~ 4 yr). South of 20°S, the intrinsic variability is, in magnitude, at least 70% of the forced variability on all time scales (i.e., $R_{\text{PSD}} = -3$ dB). In contrast, in the 45°–60°N region, the forced variability clearly dominates, mainly on decadal time scales (i.e., $R_{\text{PSD}} < -6$ dB).

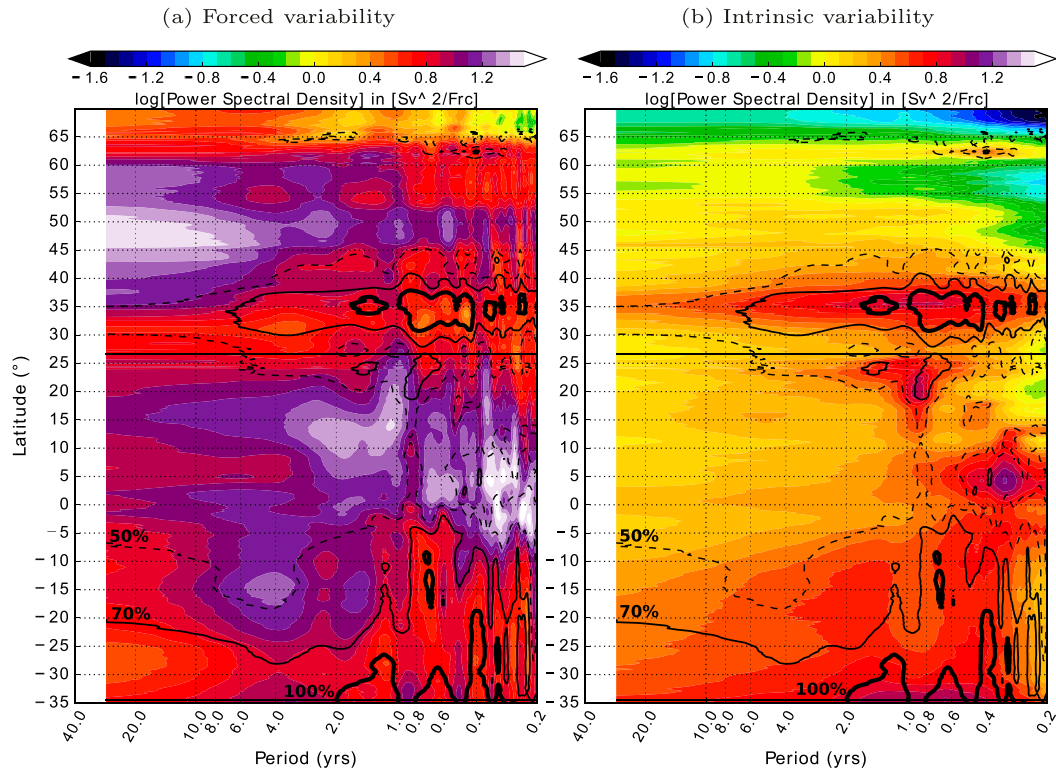


FIG. 7. PSD on a \log_{10} -scale ($\text{Sv}^2 \text{ month}$), as a function of latitude in ENSx50-occi025, from: (a) the 56-yr-long ensemble-mean monthly AMOC_{σ_2} time series ($\text{PSD}_{\text{forced}}$) and (b) 50×56 yr intrinsic monthly AMOC_{σ_2} time series ($\text{PSD}_{\text{intrinsic}}$). The ratio of the two PSDs is also computed as $R_{\text{PSD}} = 10 \log(\text{PSD}_{\text{intrinsic}}/\text{PSD}_{\text{forced}})$ (dB), and contours are shown in (a) and (b) for ratio values of -6 , -3 , and 0 dB (thin dashed, thin solid, and thick black contours, respectively) translating to an amplitude of the intrinsic variability of 50%, 70%, and 100% of the forced variability, respectively.

b. Time–latitude structure of forced and intrinsic AMOC variability

Figure 7 has shown that there is some regional coherence in the preferred time scales of the AMOC intrinsic variability in the Atlantic basin. But do these intrinsic fluctuations occur in phase over latitude ϕ ? To investigate this question, we now focus on time–latitude Hovmoeller diagrams, shown in Fig. 8. Those are based on annual means from 1) the forced part of the signal $\langle f_i(t, \phi) \rangle$, 2) the intrinsic part of the signal $f^i(t, \phi)_{i=\text{mb1}}$ from one example member in the global ensemble (ENSx50-occi025), and 3) the pure intrinsic variability from the climatological simulation (CLIM-occi025).

We find a clear meridional coherence of the AMOC fluctuations, both forced and intrinsic, over wide ranges of latitude. In-phase interannual fluctuations are clearly seen in the forced variability (Fig. 8a) in the northern and southern Atlantic with a zone of weaker meridional coherence between 25° and 35°N . A transition between northern and southern variability regimes was also detected in this latitude range by Zhang (2010), Bingham et al. (2007), and Hodson and Sutton

(2012). Those regimes might also be related to the regions identified in Fig. 7a for their different preferred time scales: interannual–subannual time scales south and decadal time scales to the north of 25°N .

Figures 8b and 8c also exhibit some clear meridionally coherent fluctuations of the interannual intrinsic AMOC variability over the entire southern basin from about 35°S to 20°N . Interestingly, Biastoch et al. (2008) reported similar large-scale, low-frequency intrinsic AMOC fluctuations in their OGCM study, and showed they were generated by low-frequency modulation of mesoscale activity in the Agulhas region.

The hypothesis that the South Atlantic is a strong source of intrinsic variability farther north is supported by the fact that the amplitude of this phenomenon drops to zero south of about 10°N in our regional North Atlantic ensemble simulation (Fig. 6a). In this simulation climatological conditions are indeed prescribed at the southern boundary (20°S) and forbid any influence of the regions located farther south on the North Atlantic intrinsic variability. Figures 8b and 8c also show that these large-scale interannual–decadal intrinsic AMOC fluctuations are coherent across the equator; this feature

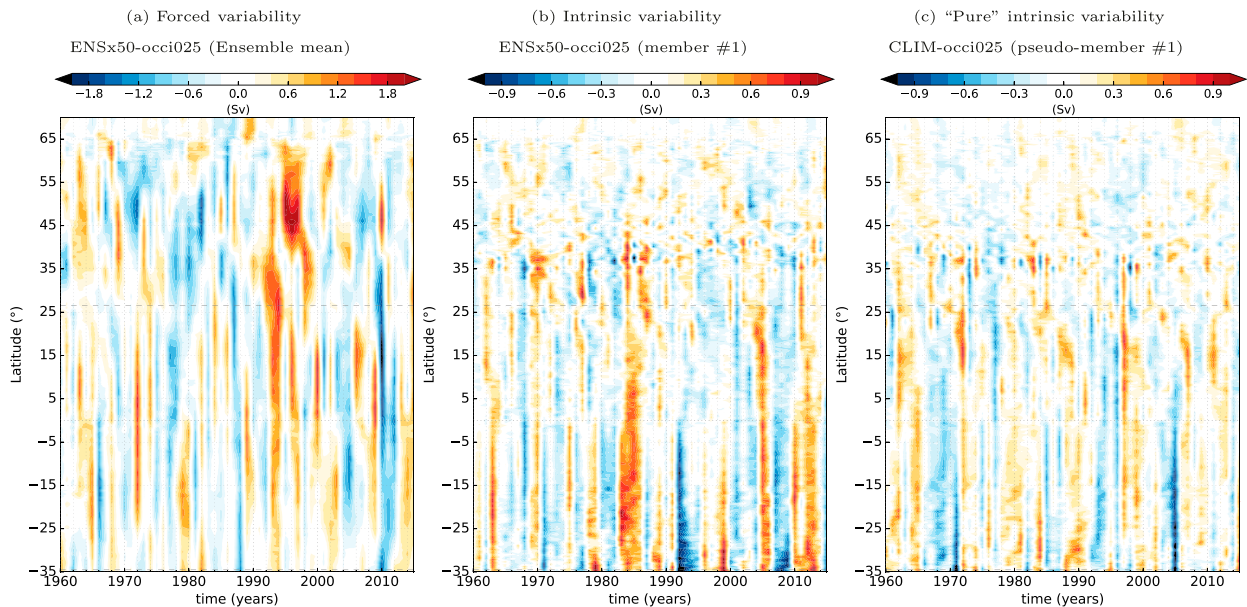


FIG. 8. Latitude–time Hovmoeller diagrams from the global ensemble ENSx50-occi025 on interannual time scales for (a) the forced AMOC (Sv) variability [i.e., the ensemble-mean signal $\langle f(t, \phi) \rangle$], (b) the intrinsic part of the signal $f'_i(t, \phi)$ from one example member, and (c) the pure intrinsic signal from a 56-yr segment of the climatological simulation CLIM-occi025.

was reported in previous OGCM studies at the same time scales by Biastoch et al. (2008) and Grégorio et al. (2015), and at seasonal time scales by Böning and Kröger (2005). This cross-equatorial transmission of relatively high-frequency AMOC anomalies is not predicted by the idealized linear wave theory proposed by Johnson and Marshall (2002). Our study and these previous references hence suggest that more complex dynamics (e.g., nonlinear, or related to western boundary processes) are involved in this interhemispheric connection, robustly found in full OGCMs.

In the 25°–45°N latitude range, which includes the mesoscale active region of the Gulf Stream, the patterns of intrinsic AMOC fluctuations look noisier but nevertheless also show some meridional coherence. This meridional coherence in the intrinsic variability becomes much weaker farther north, in contrast with the patterns in the forced variability (Fig. 8a) that can remain meridionally coherent up to 65°N with the same amplitude. Meridional coherence in the intrinsic variability might, however, exist in this latitude range (north of 45°N), but on longer time scales than those available with the ensemble approach in this study, as suggested by Grégorio et al. (2015) (e.g., their Fig. 10).

Note also that the space–time patterns of the intrinsic variability in the climatological simulation (Fig. 8c) appear qualitatively similar to how they look in the ensemble hindcast driven by interannually varying atmospheric

conditions (Fig. 8b); the varying forcing does not seem to have much influence in that regard.

c. Leading modes of forced and intrinsic AMOC variability

A latitude–time EOF analysis is now applied (Fig. 9) to retrieve the main meridionally coherent fluctuations noticed in the Hovmoeller diagrams. EOFs are computed on annual means over 1979–2015 for the forced variability (Fig. 9a), the intrinsic variability (Fig. 9b), and the pure intrinsic variability obtained in the climatological simulation (Fig. 9c; see section 3g). In practice, in Fig. 9a, the EOFs are computed from the 37-yr ensemble-mean signal (meaning a latitude–time matrix of 1021 grid points \times 37 yr). In Fig. 9b, the EOFs are computed based on the intrinsic part of the signal $f'_i(\lambda, t)$ from each member concatenated in time (50 \times 37 yr) to form a single latitude–time matrix of size 1021 grid points \times 1850 yr. In Fig. 9c, the EOFs are computed based on the pure intrinsic signal, concatenated from the climatological pseudoensemble (8 \times 37 yr) to form a latitude–time matrix of size 1021 grid points \times 296 yr. By construction, the frequency content of the signal considered in Figs. 9a–c is strictly the same. The results are robust across different latitude domains and time ranges tested for this analysis, and the EOFs are shown in Fig. 9 only if they pass North’s test on the significance of the variance explained (North et al. 1982; Björnsson and Venegas 1997).

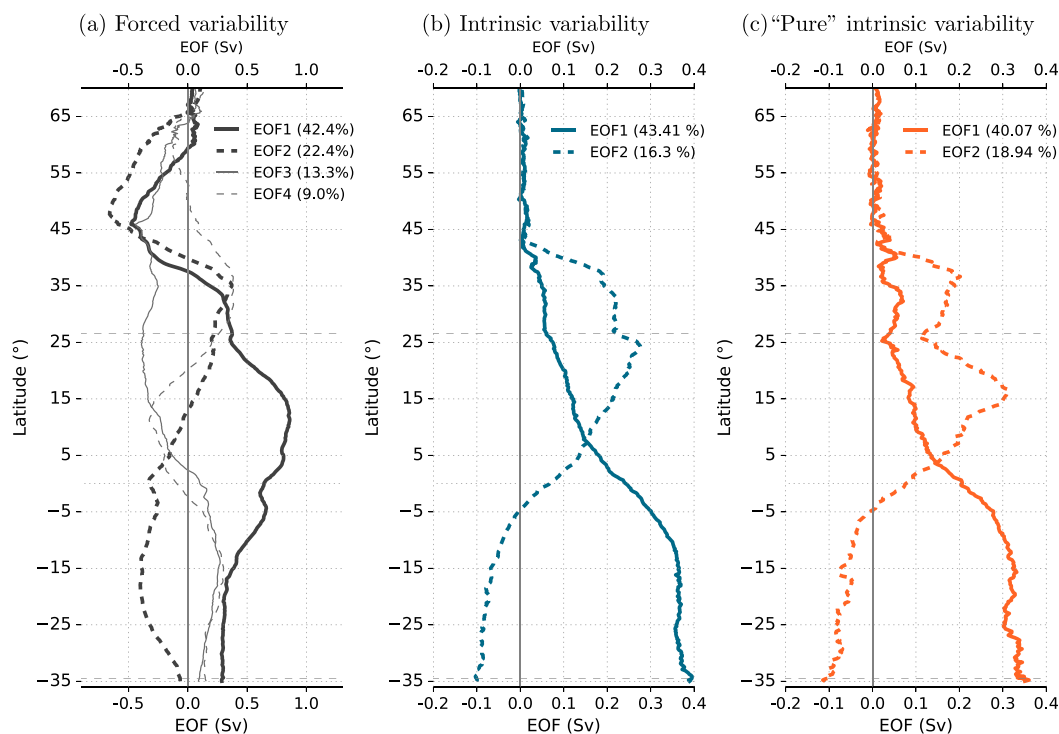


FIG. 9. The 1979–2015 latitude EOF patterns (Sv) from the global ensemble ENSx50-occi025 on interannual time scales for (a) the forced variability, (b) the intrinsic variability, and (c) the pure intrinsic variability from the climatological simulation. Details on the computation are given in section 4c. The percentage of variance explained in each case is indicated in the panel legends. The EOF patterns are presented here as the projection of the normalized principal component (PC) time series onto the initial data at each time (or, in other words, as the covariance between the two).

The two leading EOFs describing the structure of the intrinsic interannual AMOC variability are very similar in ENSx50-occi025 and CLIM-occi025, explaining about 42% and 17% of the intrinsic variance in each simulation (Figs. 9b,c). EOF1_{intrinsic} peaks homogeneously in the Southern Hemisphere and drops smoothly to zero north of the equator: this is consistent with the in-phase fluctuations highlighted previously from the Hovmoeller diagrams in the same region. Note that this mode explains almost half of the intrinsic variance over the entire basin. EOF2_{intrinsic} peaks in the midlatitudes and subtropics, between 40° and 10°N, with two local maxima. It differs slightly between ENSx50-occi025 and CLIM-occi025 in the location of the southern local maxima: the climatological simulation reveals a more pronounced maximum at 15°N (25°N in ENSx50-occi025). This difference is likely related to the presence of the additional variance peak already pointed out in the climatological simulation in Fig. 6 (also see discussion in section 3g).

Four leading EOFs are found passing North's test for the forced variability (Fig. 9a), explaining respectively 42%, 22%, 13%, and 9% of the forced variance. Note that EOF1, EOF2, and EOF3 all show a maximum in the

region north of 40°N, while none of the EOFs from the intrinsic variability explained any variance in this region. This is consistent with the variance plot in Fig. 4a and confirms the strong relationship of the AMOC fluctuations with the atmospheric variability in this region, already pointed out by, for example, Böning et al. (2006), Bingham et al. (2007), and Yeager and Danabasoglu (2014). EOF1_{forced} peaks at about 45°N, with a second peak in opposite phase around 15°N extending in the southern subtropics. EOF2_{forced} peaks both around 48°N and 20°S. Given their overlap in latitude, it is difficult to interpret further the forced EOF patterns and to attribute distinct physical processes to each of them. Some interesting additional information can, however, be deduced by comparing Fig. 9 with Fig. 10, where an EOF analysis is shown for the regional North Atlantic ensemble (ENSx10-natl025) over 1994–2012. The forced EOF modes are very similar in the regional and global ensembles. In other words, none of the forced EOF modes are missing in the regional ensemble, where climatological conditions have been applied at the southern lateral boundary (20°S), thus filtering out any possible remote (southern) influence on the AMOC variability. It thus confirms the idea that the

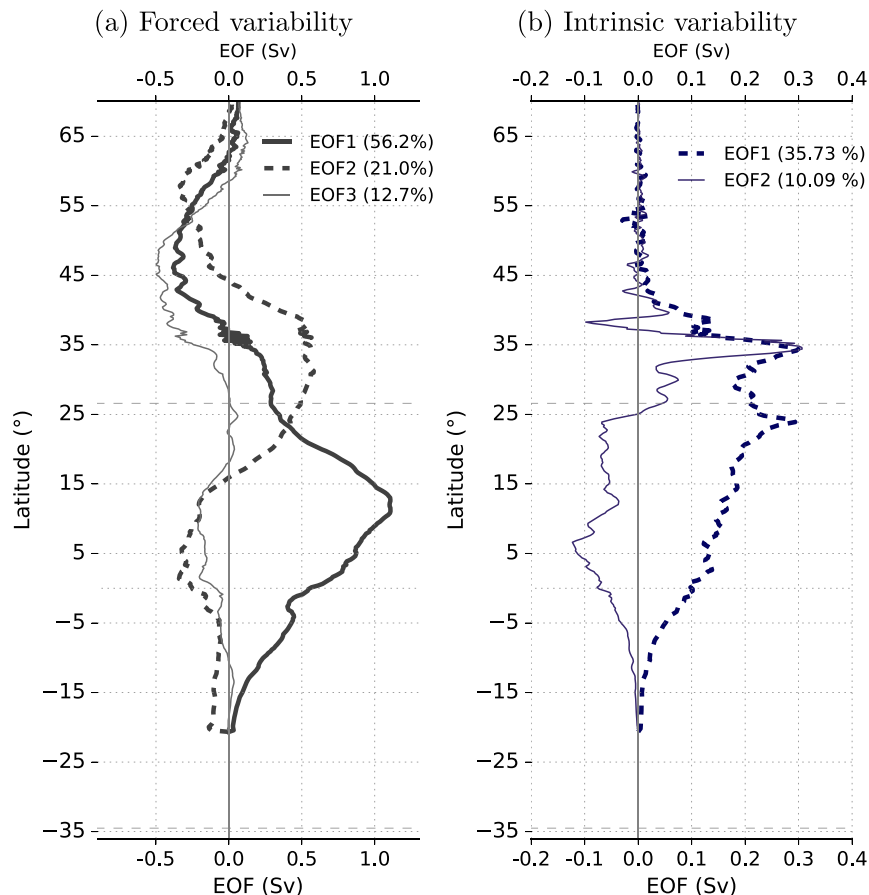


FIG. 10. The 1994–2012 latitude EOF patterns (Sv) from the North Atlantic regional ensemble ENSx10-natl025 on interannual time scales for (a) the forced variability and (b) the intrinsic variability. Details on the computation are given in section 4c. The southern boundary of the regional configuration is at 20°S. The percentage of variance explained in each case is indicated in the panel legends. The EOF patterns are presented here as the projection of the normalized PC time series onto the initial data at each time (or, in other words, as the covariance between the two).

atmospheric forcing associated with these forced modes acts locally. In contrast, only EOF2_{intrinsic} is found both in the regional and global ensembles. EOF1_{intrinsic}, which explains 43% of the intrinsic variance in the global ensemble and corresponds to in-phase fluctuations in the Southern Hemisphere, is missing in the regional ensemble. It is thus another suggestion that the intrinsic fluctuations associated with EOF1_{intrinsic} are generated in, and propagate from, the southern end of the basin, possibly related to the modulation of mesoscale activity in the Brazil–Malvinas Confluence region and/or the Agulhas region as was suggested by, for example, [Biaostoch et al. \(2008\)](#) and [Dong et al. \(2015\)](#). Other authors have also suggested a potential remote forcing influence of the surface wind stress in the Southern Ocean on interannual AMOC variability (e.g., [Yeager and Danabasoglu 2014](#)). Our results do not confirm or rule out this proposed mechanism, but we do not find any evidence for a forced

mode that would propagate from the south of the basin, phase locked in all the members. On the contrary, we do find such a southerly mode but in the intrinsic part of the AMOC variability (i.e., fluctuations having different time phases in the different members). It suggests that if some AMOC variability is indeed induced remotely by the atmospheric forcing in the Southern Ocean, the propagation mechanism is such that it generates intrinsic AMOC fluctuations, differing in phase from one member to another. Alternatively, it is also possible that a forcing mechanism by the Southern Ocean operates at longer time scales than those we can retrieve from our analysis (>30 yr).

5. Summary and conclusions

Our study investigates the nature of interannual–decadal variability of the AMOC, making use of large ensembles of sea ice–ocean hindcasts at eddy-permitting

resolution ($1/4^\circ$) performed in the OCCIPUT project. This modeling approach was for the first time applied to a global OGCM at eddying resolution with $N = 50$ ensemble members (Bessières et al. 2017).

This approach provides a consistent framework to study and quantify the fraction of the AMOC variability that is generated from ocean intrinsic processes relative to that driven by the atmospheric variability imposed through the surface boundary conditions. The atmospherically forced variability is estimated from the fluctuations of the ensemble mean, whereas the intrinsic variability is estimated from the ensemble spread. On the time scales considered in this study (2–28 yr), the atmospherically forced AMOC variability exceeds the intrinsic variability in the entire Atlantic basin, but we find that the intrinsic contribution reaches a significant fraction of the variability in several regions. The amplitude ratio between intrinsic and forced variability can be up to 100% in the southern Atlantic, and it peaks twice at 60% in the Northern Hemisphere midlatitudes, close to the location of the RAPID observational array at 26.5°N .

We also find that despite the chaotic nature of the intrinsic variability, it shows a clear meridional coherence south of about 25°N , mostly on subannual–short interannual time scales. Our EOF analysis in fact suggests the existence of two main regional modes explaining in total about 60% of the intrinsic variance. The second EOF explains about 17% of the intrinsic variance over the Atlantic Ocean and seems to be generated within the North Atlantic midlatitude region. In contrast, the first EOF explains 43% of the intrinsic variance in the Atlantic in the form of coherent fluctuations south of the equator. Because this mode vanishes in the regional North Atlantic simulation where climatological conditions were applied at the southern boundary at 20°N , it suggests a source of intrinsic AMOC variability in the southern Atlantic. This is consistent with previous discussions in the literature mentioning the possible role of the mesoscale-active regions of the Agulhas Current, the Brazil–Malvinas Confluence, and/or of the Southern Ocean on AMOC variability, including on interannual–decadal time scales (Bjostoch et al. 2008; Grégorio et al. 2015; Dong et al. 2015; Yeager and Danabasoglu 2014). Our results also show a strong constraint exerted by the atmospheric variability on the AMOC variability north of 40°N . These forced AMOC fluctuations are coherent in latitude over the region and favor time scales in the subdecadal–decadal range, consistent with, for example, Böning et al. (2006), Bingham et al. (2007), and Yeager and Danabasoglu (2014), who previously pointed out the role of convection in the Labrador Sea, and of surface forcing by the NAO, in driving the AMOC in the North Atlantic.

In addition, this study shows that the amount, meridional distribution, and space–time spectral characteristics of intrinsic variability remain fairly unchanged under realistic atmospheric forcing, compared to the “pure intrinsic” variability from the climatological simulation. Only in one region, around 15°N , did we find a noticeable difference between the climatological run and the ensemble hindcast in the amount of intrinsic variance (see discussion in section 3g). In many aspects, our results are very consistent with the previous study by Grégorio et al. (2015) based on such a climatological simulation. Note, however, that only an ensemble approach can provide a time-dependent estimate of the amplitude of the intrinsic variability and a simultaneous analysis of both the forced and intrinsic contributions to compare their structures and their relative importance.

Overall, the substantial amount of intrinsic AMOC variability that we have detected in some regions relative to the atmospherically forced contribution raises important questions on how we should assess AMOC variability from model simulations and observational records. Our study advocates to better take into account the uncertainty attached to the variability deduced from time series from single simulations. It also questions the significance of trends or low-frequency variations that we might try to detect or predict and attribute to the changing climate. In regions where the amount of intrinsic ocean noise is as high as the atmospherically driven variability, it might be difficult to retrieve significant trends or decadal variations from 10- or 20-yr-long observational records, as is the case for the 2004–12 RAPID–MOCHA record (e.g., Baehr et al. 2007). The issue has also been investigated in parallel in the OCCIPUT project in Sérazin et al. (2017), focusing on the ocean heat content (OHC). Their study highlights different areas where large-scale regional OHC trends computed over the 1980–2010 period cannot be unambiguously attributed to the atmospheric forcing, for example, in the subpolar North Pacific and in the South Atlantic.

Finally, our results raise the question of the potential impact on the atmosphere of this spontaneous, chaotic variability of the AMOC arising in eddy-permitting OGCMs. This AMOC noise is all the more likely to have an impact that it is regionally coherent and affecting interannual and decadal time scales. Given that climate ocean–atmosphere coupled simulations have been mostly based on laminar (noneddying) ocean models up to now (e.g., CMIP5), one can wonder how much they have actually missed of the climate variability from intrinsic oceanic sources on low-frequency time scales. Ensembles of coupled simulations using eddy-permitting ocean models will be needed to further investigate this question in a framework where ocean and

atmosphere are freely interacting. Results from ocean-only ensemble simulations, such as the OCCIPUT ensemble presented here, are crucial in order to better understand the eddying-ocean low-frequency chaotic behavior and prepare the next (coupled) step.

Acknowledgments. We wish to thank the three reviewers for their careful reading and constructive comments and suggestions that lead to significant improvements in the manuscript. The dataset produced for this study is available upon request (contact: thierry.penduff@cns.fr). EOF computations were performed with the Python package developed by A. Dawson (<https://doi.org/10.5334/jors.122>). We acknowledge that the results of this research have been achieved using the PRACE Research Infrastructure resource CURIE based in France at TGCC. The support of the TGCC-CCRT hotline from CEA, France, to the technical work is gratefully acknowledged. Some of the computations presented in this study were performed at TGCC under allocations granted by GENCI. This work is a contribution to the OCCIPUT project (<http://meom-group.github.io/projects/occiput/>) funded by the French Agence Nationale de la Recherche (ANR) through Contract ANR-13-BS06-0007-01, and to the PIRATE project (<https://sealevel.jpl.nasa.gov/science/ostscienceteam/scientistlinks/scientificinvestigations2017/penduff/>) funded by the Centre National d'Études Spatiales (CNES) through the Ocean Surface Topography Science Team (OST/ST). This work also benefited from many interactions with the DRAKKAR ocean modeling international coordination network (GDRI) established between CNRS, NOCS, GEOMAR, and IFREMER, and with the SANGOMA and CHAOCEAN projects.

APPENDIX

Error on the Variance Estimator of a Finite-Size Ensemble

The ensemble spread $\varepsilon^2(t)$, as defined in this study (section 2d), is a variance estimator, or sample variance, computed each year from a finite-size sample ($N = 50$). A sample variance is itself a random variable, and, as such, its distribution can be characterized by a variance γ^2 expressed as (e.g., Mood et al. 1974, p. 229)

$$\gamma^2 = \text{var}(S^2) = \frac{1}{N} \left[\mu_4 - \frac{N-3}{N-1} (\sigma^2)^2 \right], \quad (\text{A1})$$

where S^2 is the sample variance, σ^2 is the population variance, and μ_4 is its fourth central moment.

We use the interval $[\varepsilon^2 - 2\gamma, \varepsilon^2 + 2\gamma]$ as the 95% confidence interval to take into account the error made each year on ε^2 due to the finite-size ensemble.

REFERENCES

- Ansorge, I. J., and Coauthors, 2014: Basin-wide oceanographic array bridges the South Atlantic. *Eos, Trans. Amer. Geophys. Union*, **95**, 53–54, <https://doi.org/10.1002/2014EO060001>.
- Baehr, J., H. Haak, S. Alderson, S. A. Cunningham, J. H. Jungclauss, and J. Marotzke, 2007: Timely detection of changes in the meridional overturning circulation at 26°N in the Atlantic. *J. Climate*, **20**, 5827–5841, <https://doi.org/10.1175/2007JCLI1686.1>.
- Barnier, B., and Coauthors, 2006: Impact of partial steps and momentum advection schemes in a global ocean circulation model at eddy-permitting resolution. *Ocean Dyn.*, **56**, 543–567, <https://doi.org/10.1007/s10236-006-0082-1>.
- Bessières, L., and Coauthors, 2017: Development of a probabilistic ocean modelling system based on NEMO 3.5: Application at eddying resolution. *Geosci. Model Dev.*, **10**, 1091–1106, <https://doi.org/10.5194/gmd-10-1091-2017>.
- Biastoch, A., C. W. Böning, and J. R. E. Lutjeharms, 2008: Agulhas leakage dynamics affects decadal variability in Atlantic overturning circulation. *Nature*, **456**, 489–492, <https://doi.org/10.1038/nature07426>.
- Bingham, R. J., C. W. Hughes, V. Roussenov, and R. G. Williams, 2007: Meridional coherence of the North Atlantic meridional overturning circulation. *Geophys. Res. Lett.*, **34**, L23606, <https://doi.org/10.1029/2007GL031731>.
- Björnsson, H., and S. A. Venegas, 1997: A manual for EOF and SVD analyses of climatic data. McGill University C²GCR Rep. 97-1, 52 pp., <http://www.jsg.utexas.edu/fu/files/EOFSVD.pdf>.
- Böning, C. W., and J. Kröger, 2005: Seasonal variability of deep currents in the equatorial Atlantic: A model study. *Deep-Sea Res. I*, **52**, 99–121, <https://doi.org/10.1016/j.dsr.2004.06.015>.
- , M. Scheinert, J. Dengg, A. Biastoch, and A. Funk, 2006: Decadal variability of subpolar gyre transport and its reverberation in the North Atlantic overturning. *Geophys. Res. Lett.*, **33**, L21S01, <https://doi.org/10.1029/2006GL026906>.
- Brankart, J.-M., G. Candille, F. Garnier, C. Calone, A. Melet, P.-A. Bouttier, P. Brasseur, and J. Verron, 2015: A generic approach to explicit simulation of uncertainty in the NEMO ocean model. *Geosci. Model Dev.*, **8**, 1285–1297, <https://doi.org/10.5194/gmd-8-1285-2015>.
- Buckley, M. W., and J. Marshall, 2016: Observations, inferences, and mechanisms of the Atlantic meridional overturning circulation: A review. *Rev. Geophys.*, **54**, 5–63, <https://doi.org/10.1002/2015RG000493>.
- , D. Ferreira, J.-M. Campin, J. Marshall, and R. Tulloch, 2012: On the relationship between decadal buoyancy anomalies and variability of the Atlantic meridional overturning circulation. *J. Climate*, **25**, 8009–8030, <https://doi.org/10.1175/JCLI-D-11-00505.1>.
- Cleveland, W. S., and S. J. Devlin, 1988: Locally weighted regression: An approach to regression analysis by local fitting. *J. Amer. Stat. Assoc.*, **83**, 596–610, <https://doi.org/10.1080/01621459.1988.10478639>.
- Danabasoglu, G., 2008: On multidecadal variability of the Atlantic meridional overturning circulation in the Community Climate

- System Model version 3. *J. Climate*, **21**, 5524–5544, <https://doi.org/10.1175/2008JCLI2019.1>.
- Deser, C., M. A. Alexander, S.-P. Xie, and A. S. Phillips, 2010: Sea surface temperature variability: Patterns and mechanisms. *Annu. Rev. Mar. Sci.*, **2**, 115–143, <https://doi.org/10.1146/annurev-marine-120408-151453>.
- Dijkstra, H. A., and M. Ghil, 2005: Low-frequency variability of the large-scale ocean circulation: A dynamical systems approach. *Rev. Geophys.*, **43**, RG3002, <https://doi.org/10.1029/2002RG000122>.
- Dong, S., G. Goni, and F. Bringas, 2015: Temporal variability of the South Atlantic meridional overturning circulation between 20°S and 35°S. *Geophys. Res. Lett.*, **42**, 7655–7662, <https://doi.org/10.1002/2015GL065603>.
- Duchez, A., P. Courtois, E. Harris, S. A. Josey, T. Kanzow, R. Marsh, D. Smeed, and J.-M. Hirschi, 2016: Potential for seasonal prediction of Atlantic sea surface temperatures using the RAPID array at 26°N. *Climate Dyn.*, **46**, 3351–3370, <https://doi.org/10.1007/s00382-015-2918-1>.
- Dussin, R., B. Barnier, L. Brodeau, and J. M. Molines, 2016: The making of DRAKKAR forcing set DFS5. DRAKKAR/My-Ocean Rep. 01-04-16, 34 pp., https://www.drakkar-ocean.eu/publications/reports/report_DFS5v3_April2016.pdf.
- Eade, R., D. Smith, A. Scaife, E. Wallace, N. Dunstone, L. Hermanson, and N. Robinson, 2014: Do seasonal-to-decadal climate predictions underestimate the predictability of the real world? *Geophys. Res. Lett.*, **41**, 5620–5628, <https://doi.org/10.1002/2014GL061146>.
- Enfield, D. B., A. M. Mestas-Núñez, and P. J. Trimble, 2001: The Atlantic multidecadal oscillation and its relation to rainfall and river flows in the continental U.S. *Geophys. Res. Lett.*, **28**, 2077–2080, <https://doi.org/10.1029/2000GL012745>.
- Frierson, D. M., and Coauthors, 2013: Contribution of ocean overturning circulation to tropical rainfall peak in the Northern Hemisphere. *Nat. Geosci.*, **6**, 940–944, <https://doi.org/10.1038/ngeo1987>.
- Garzoli, S., and Coauthors, 2012: South Atlantic meridional overturning circulation (SAMOC)—Fourth workshop. *CLIVAR Exchanges*, No. 58, International CLIVAR Project Office, Southampton, United Kingdom, 2–4.
- Grégorio, S., T. Penduff, G. Sérazin, J. M. Molines, B. Barnier, and J. Hirschi, 2015: Intrinsic variability of the Atlantic meridional overturning circulation at interannual-to-multidecadal time scales. *J. Phys. Oceanogr.*, **45**, 1929–1948, <https://doi.org/10.1175/JPO-D-14-0163.1>.
- Haarsma, R., and Coauthors, 2016: High Resolution Model Intercomparison Project (HighResMIP v1.0) for CMIP6. *Geosci. Model Dev.*, **9**, 4185–4208, <https://doi.org/10.5194/gmd-9-4185-2016>.
- Hirschi, J., J. Baehr, J. Marotzke, J. Stark, S. Cunningham, and J.-O. Beismann, 2003: A monitoring design for the Atlantic meridional overturning circulation. *Geophys. Res. Lett.*, **30**, 1413, <https://doi.org/10.1029/2002GL016776>.
- , A. T. Blaker, B. Sinha, A. Coward, B. de Cuevas, S. Alderson, and G. Madec, 2013: Chaotic variability of the meridional overturning circulation on subannual to interannual timescales. *Ocean Sci.*, **9**, 805–823, <https://doi.org/10.5194/os-9-805-2013>.
- Hodson, D. L., and R. T. Sutton, 2012: The impact of resolution on the adjustment and decadal variability of the Atlantic meridional overturning circulation in a coupled climate model. *Climate Dyn.*, **39**, 3057–3073, <https://doi.org/10.1007/s00382-012-1309-0>.
- Johnson, H., and D. Marshall, 2002: A theory for the surface Atlantic response to thermohaline variability. *J. Phys. Oceanogr.*, **32**, 1121–1132, [https://doi.org/10.1175/1520-0485\(2002\)032<1121:ATFTSA>2.0.CO;2](https://doi.org/10.1175/1520-0485(2002)032<1121:ATFTSA>2.0.CO;2).
- Kerr, R. A., 2000: A North Atlantic climate pacemaker for the centuries. *Science*, **288**, 1984–1985, <https://doi.org/10.1126/science.288.5473.1984>.
- Levitus, S., and Coauthors, 1998: *Introduction*. Vol. 1, World Ocean Database 1998, NOAA Atlas NESDIS 18, 346 pp.
- Lherminier, P., H. Mercier, C. Gourcuff, M. Alvarez, S. Bacon, and C. Kermabon, 2007: Transports across the 2002 Greenland–Portugal Ovide section and comparison with 1997. *J. Geophys. Res.*, **112**, C07003, <https://doi.org/10.1029/2006JC003716>.
- Lozier, M. S., and Coauthors, 2017: Overturning in the Subpolar North Atlantic Program: A new international ocean observing system. *Bull. Amer. Meteor. Soc.*, **98**, 737–752, <https://doi.org/10.1175/BAMS-D-16-0057.1>.
- Madec, G., 2012: NEMO ocean engine. Pôle de modélisation de l’Institute Pierre-Simon Laplace Rep. 27, 396 pp., https://www.nemo-ocean.eu/wp-content/uploads/NEMO_book.pdf.
- Marshall, J., A. Donohoe, D. Ferreira, and D. McGee, 2014: The ocean’s role in setting the mean position of the inter-tropical convergence zone. *Climate Dyn.*, **42**, 1967–1979, <https://doi.org/10.1007/s00382-013-1767-z>.
- Mood, A., F. Graybill, and D. Boes, 1974: *Introduction to the Theory of Statistics*. 3rd ed. McGraw-Hill Series in Probability and Statistics, McGraw-Hill, 480 pp.
- North, G. R., T. L. Bell, R. F. Cahalan, and F. J. Moeng, 1982: Sampling errors in the estimation of empirical orthogonal functions. *Mon. Wea. Rev.*, **110**, 699–706, [https://doi.org/10.1175/1520-0493\(1982\)110<0699:SEITEO>2.0.CO;2](https://doi.org/10.1175/1520-0493(1982)110<0699:SEITEO>2.0.CO;2).
- Penduff, T., M. Juza, B. Barnier, J. Zika, W. K. Dewar, A.-M. Treguier, J.-M. Molines, and N. Audiffren, 2011: Sea level expression of intrinsic and forced ocean variabilities at interannual time scales. *J. Climate*, **24**, 5652–5670, <https://doi.org/10.1175/JCLI-D-11-00077.1>.
- , and Coauthors, 2014: Ensembles of eddy ocean simulations for climate. *CLIVAR Exchanges*, No. 65, International CLIVAR Project Office, Southampton, United Kingdom, 26–29.
- Reichler, T., J. Kim, E. Manzini, and J. Kröger, 2012: A stratospheric connection to Atlantic climate variability. *Nat. Geosci.*, **5**, 783–787, <https://doi.org/10.1038/ngeo1586>.
- Roberts, C. D., and Coauthors, 2013a: Atmosphere drives recent interannual variability of the Atlantic meridional overturning circulation at 26.5°N. *Geophys. Res. Lett.*, **40**, 5164–5170, <https://doi.org/10.1002/grl.50930>.
- , F. K. Garry, and L. C. Jackson, 2013b: A multimodel study of sea surface temperature and subsurface density fingerprints of the Atlantic meridional overturning circulation. *J. Climate*, **26**, 9155–9174, <https://doi.org/10.1175/JCLI-D-12-00762.1>.
- Sérazin, G., T. Penduff, S. Grégorio, B. Barnier, J.-M. Molines, and L. Terray, 2015: Intrinsic variability of sea level from global ocean simulations: Spatiotemporal scales. *J. Climate*, **28**, 4279–4292, <https://doi.org/10.1175/JCLI-D-14-00554.1>.
- , B. Meyssignac, T. Penduff, L. Terray, B. Barnier, and J.-M. Molines, 2016: Quantifying uncertainties on regional sea level change induced by multidecadal intrinsic oceanic variability. *Geophys. Res. Lett.*, **43**, 8151–8159, <https://doi.org/10.1002/2016GL069273>.
- , and Coauthors, 2017: A global probabilistic study of the ocean heat content low-frequency variability: Atmospheric forcing versus oceanic chaos. *Geophys. Res. Lett.*, **44**, 5580–5589, <https://doi.org/10.1002/2017GL073026>.

- Sévellec, F., and T. Huck, 2015: Theoretical investigation of the Atlantic multidecadal oscillation. *J. Phys. Oceanogr.*, **45**, 2189–2208, <https://doi.org/10.1175/JPO-D-14-0094.1>.
- Shin, S.-I., and P. D. Sardeshmukh, 2011: Critical influence of the pattern of tropical ocean warming on remote climate trends. *Climate Dyn.*, **36**, 1577–1591, <https://doi.org/10.1007/s00382-009-0732-3>.
- Smeed, D. A., and Coauthors, 2014: Observed decline of the Atlantic meridional overturning circulation 2004–2012. *Ocean Sci.*, **10**, 29–38, <https://doi.org/10.5194/os-10-29-2014>.
- Taylor, K. E., 2001: Summarizing multiple aspects of model performance in a single diagram. *J. Geophys. Res.*, **106**, 7183–7192, <https://doi.org/10.1029/2000JD900719>.
- Ting, M., Y. Kushnir, R. Seager, and C. Li, 2009: Forced and internal twentieth-century SST trends in the North Atlantic. *J. Climate*, **22**, 1469–1481, <https://doi.org/10.1175/2008JCLI2561.1>.
- Xu, X., E. P. Chassignet, W. E. Johns, W. J. Schmitz, and E. J. Metzger, 2014: Intraseasonal to interannual variability of the Atlantic meridional overturning circulation from eddy-resolving simulations and observations. *J. Geophys. Res. Oceans*, **119**, 5140–5159, <https://doi.org/10.1002/2014JC009994>.
- Yeager, S., and G. Danabasoglu, 2014: The origins of late-twentieth-century variations in the large-scale North Atlantic circulation. *J. Climate*, **27**, 3222–3247, <https://doi.org/10.1175/JCLI-D-13-00125.1>.
- Zhang, R., 2010: Latitudinal dependence of Atlantic meridional overturning circulation (AMOC) variations. *Geophys. Res. Lett.*, **37**, L16703, <https://doi.org/10.1029/2010GL044474>.
- , and T. L. Delworth, 2005: Simulated tropical response to a substantial weakening of the Atlantic thermohaline circulation. *J. Climate*, **18**, 1853–1860, <https://doi.org/10.1175/JCLI3460.1>.
- Zhao, J., and W. Johns, 2014: Wind-forced interannual variability of the Atlantic meridional overturning circulation at 26.5°N. *J. Geophys. Res. Oceans*, **119**, 2403–2419, <https://doi.org/10.1002/2013JC009407>.